

Hyperenrichment of gold in pyrite induced by solid-state transportation

Haiyang Xian^{1,2}, Hongping He^{1,2,3✉}, Jianxi Zhu^{1,2}, Kunfeng Qiu⁴, Yang Li⁵, Yiping Yang^{1,2}, Jieqi Xing^{1,2,3}, Wei Tan^{1,2}, Akira Tsuchiyama^{1,2,6}, Masahiro Yastake⁷, Satomi Enju⁸, Akira Miyake⁹ & Runliang Zhu^{1,2}

The hyperenrichment of gold is critical for the formation of high-grade gold deposits in orogenic systems, where gold enrichment can reach several percent. However, many details on the nature of the hyperenrichment mechanism remain unclear. Here we show a “self-purification” model that could explain the hyperenrichment of gold from nanoparticles to veinlets in deformed pyrite. The three-dimensional spatial relationship and coexistence of gold nanoparticles and veinlets indicate a direct transformation from the former to the latter in solid-state. Theoretical evaluation reveals that this transformation involves a thermodynamically favorable self-purification process. We thus propose that deformation/thermo drives the transport of gold nanoparticles towards veinlets in pyrite through atomic diffusion. This deformation/thermo-driven model is applicable to any deformed nano-gold-bearing pyrite and explains how solid-state transport can effectively concentrate gold to a very high grade. Similar mechanisms may have broad implications in both ore-forming and beneficiation processes.

¹CAS Key Laboratory of Mineralogy and Metallogeny/Guangdong Provincial Key Laboratory of Mineral Physics and Materials, Guangzhou Institute of Geochemistry, Chinese Academy of Sciences (CAS), Guangzhou 510640, China. ²CAS Center for Excellence in Deep Earth Science, Guangzhou 510640, China. ³University of Chinese Academy of Sciences, Beijing 100049, China. ⁴State Key Laboratory of Geological Processes and Mineral Resources, School of Earth Sciences and Resources, China University of Geosciences, Beijing 100083, China. ⁵State Key Laboratory of Lithospheric Evolution, Institute of Geology and Geophysics, Chinese Academy of Sciences, Beijing 100029, China. ⁶Research Organization of Science and Technology, Ritsumeikan University, Kusatsu, Shiga 525-8577, Japan. ⁷Japan Synchrotron Radiation Research Institute, Hyogo 679-5198, Japan. ⁸Department of Mathematics, Physics, and Earth Sciences, Graduate School of Science and Engineering, Ehime University, Matsuyama, Ehime 790-8577, Japan. ⁹Department of Earth and Planetary Sciences, Graduate School of Science, Kyoto University, Kitashirakawa-Oiwakecho, Sakyo-ku, Kyoto 606-8502, Japan. ✉email: hehp@gig.ac.cn

Orogenic Au deposits contribute ~75% of the historically recovered Au^{1–3}. The average grade of gold in orogenic deposits ranges from several to tens of ppm at the deposit scale, but local concentrations can reach several percent^{2,4}. Such a high grade of gold at the local scale has difficulty explaining the direct deposition of Au from hydrothermal fluids since the over-saturation deposition can only reach parts per million levels⁵. Thus, colloidal transport of gold was proposed as an alternative mechanism for forming bonanza vein gold⁶. Recent studies have revealed the occurrence of gold nanoparticles that can transport in colloids and be further enriched^{4,7,8}. Additionally, in situ observation of gold colloids in black smoker hydrothermal fluids confirmed the long-standing hypothesis that gold may undergo colloidal transport in hydrothermal fluids⁹. In addition, dissolution–reprecipitation and Ostwald ripening can also transport and coarsen gold nanoparticles, causing hyperenrichment¹⁰.

However, the aforementioned mechanisms that involve aqueous processes are hard to explain the occurrence of gold-bearing veinlets filling in fractures of pyrites where aqueous processes are absent. The gold concentration can reach 90 wt% at the sub-micro scale in these veinlets. The distinct edges of these gold-bearing veinlets and the unreacted surfaces of the vacant fractures in pyrite indicate that the gold-bearing veinlets did not experience aqueous processes. Therefore, other mechanisms that involve non-aqueous processes may explain the bonanza filling in the fractures of pyrite crystals.

Here we present mineralogical evidence for a solid-state transport model that could well explain the hyper-enriched gold-bearing veinlets in pyrite. In this model, gold nanoparticles first precipitate from fluids at a low grade and then are transported in solid-state via atomic diffusion and eventually enriched in deformed pyrite fractures.

Results

Samples were collected from the Dakaitou deposit of the Linglong goldfield (Fig. 1a), Jiaodong gold province, China (Supplementary Fig. 1). The Jiaodong gold province, within the eastern margin of the North China Block and the translated north-eastern edge of the South China Block¹¹, hosts relatively young gold ores (ca. 120 Ma) in the terranes that are billions of years older (ca. 2.9 – 1.9 Ga)¹². The Jiaodong gold deposits are regarded as orogenic gold deposits³, though “Jiaodong-type” gold deposits also have been proposed¹³. The ore minerals in the samples are primarily euhedral-subhedral pyrite that occurred in quartz veins (Supplementary Fig. 2a and Supplementary Table 1). Gold in the ore mineral pyrite mainly occurs as gold-bearing veinlets in microfractures (Fig. 1b–e) and along grain boundaries (Supplementary Fig. 2b–c).

Micro veinlets with a width range between ~100 nm and ~5 μm were observed in the scanning electron microscope (SEM) images of backscatter electrons (Fig. 1b–e). The energy dispersive spectroscopy (EDS) elemental maps (Supplementary Fig. 3) display two types of veinlets. One type is deficient in Au (Supplementary Fig. 3a), while the other is Au-rich (Supplementary Fig. 3c). The two types of veinlets (Supplementary Fig. 3) were also readily distinguished by their compositions determined by the linear attenuation coefficients of X-rays from synchrotron radiation-x-ray computed tomography (SR-XCT) (i.e., the contrast in Fig. 1e, Supplementary Figs. 4 and 5) and by EDS maps from scanning transmission electron microscopy (STEM) (Fig. 2a–d).

The three-dimensional distribution of the gold-bearing veinlets in the host pyrite shows that most distribute along pyrite within fractures and are connected (Fig. 1e and Supplementary Movie 1). Pyrite on both sides of veinlets shows the same crystallographic orientation (Fig. 2f–g). Blebs and discontinued veinlets are also present in the host pyrite (Fig. 1e, Supplementary Fig. 4 and

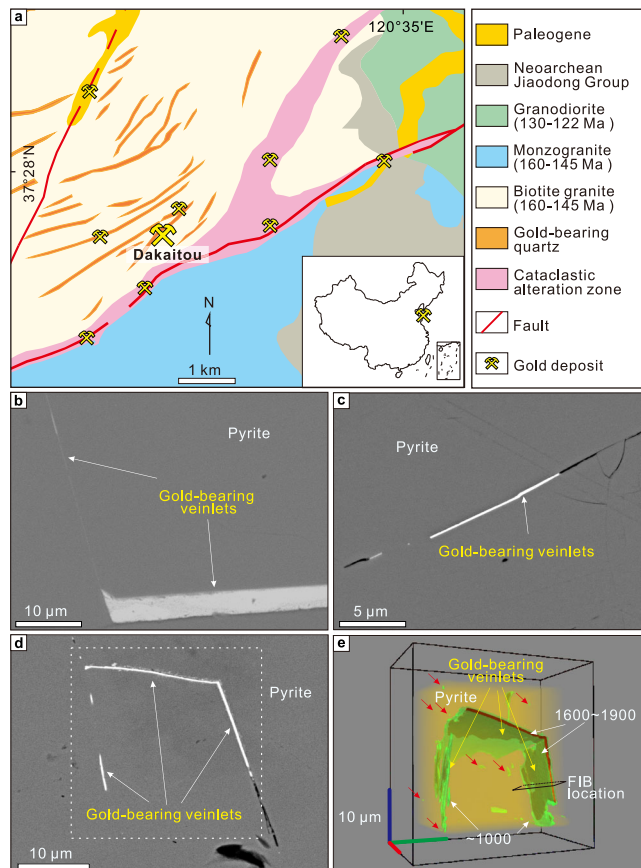


Fig. 1 Geological background and gold occurrences in pyrite from the Dakaitou deposit in Jiaodong gold province, China. **a** Simplified geologic map of the Linglong goldfield in Jiaodong gold province, China. Modified after ref. 12. **b–d** Backscattering scanning electron micrographs showing the occurrence of gold-bearing veinlets in the pyrite collected from the Dakaitou gold deposit. **e** SR-XCT three-dimensional distributions of gold-bearing veinlets in the Dakaitou pyrite (box size 35 μm × 20 μm × 35 μm). The sample used for SR-XCT analysis was cut using a focused ion beam in the zone marked by a dashed rectangle in **d**. The red arrows in **e** indicate gold-bearing islets in closed space and discontinuity of the veinlets in the pyrite. The numbers are the contrast intensity of the X-ray computed tomogram. The yellow, brown, and green colored zones denote pyrite, gold, and silver tellurosulfide. The marked focus ion beam cutting location shows the sampling position for further TEM observation in Fig. 2.

Supplementary Movie 2). The electron diffraction patterns (Fig. 2f–i) and standard-based quantitative EDS (Supplementary Figs. 6–8 and Supplementary Table 2) show that the gold-bearing veinlets are composed of Au–Ag alloy with Ag/Au ratios ranging from 0.08 to 2.7. An unknown Ag–Fe–Te–S mineral veinlets with a formula of Ag₈Fe_{0.94}Te_{4.83}S_{3.99} (stoichiometric Ag₈FeTe₅S₄) also occurs in the pyrite (Supplementary Fig. 10 and Supplementary Table 3). A high-resolution transmission electron micrograph of the host pyrite (Fig. 2e) shows that Te-bearing nanoparticles (~5–50 nm), with the same *d*-spacings at 3.2 and 1.9 Å as the unknown Ag–Fe–Te–S mineral (Fig. 2h–i), are present in the host pyrite. However, the elemental maps of the pyrite hosting these nanoparticles exhibit no variation in the scanning area (Supplementary Fig. 9), suggesting an even dispersion of nanoparticles in pyrite. Au–Ag alloy nanoparticles occur at the end of the veinlet close to the vacant space (Fig. 2j–m).

The calculated formation enthalpy (ΔH_f) of the atomic substitution of both Au and Ag in different Fe layers (Fig. 3) shows that ΔH_f decreases as the gold and silver atoms move from the bulk to

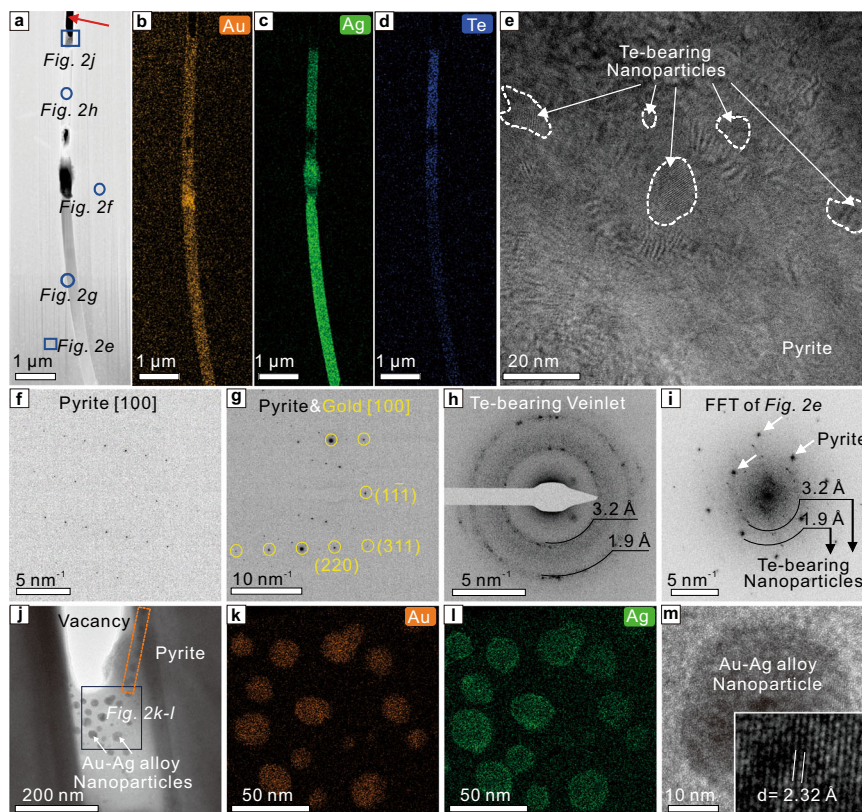


Fig. 2 TEM analyses of the gold-bearing pyrite from the Dakaitou deposit in Jiaodong gold province, China. High-angle annular dark-field scanning transmission micrograph (a), energy-dispersive spectroscopic elemental maps (b–d and k–l), high-resolution transmission electron micrographs (e, j, and m), electron diffraction patterns (f–i) of the Dakaitou gold-bearing pyrite. The locations of the electron diffraction patterns and high-resolution transmission electron micrographs are marked in a. The elemental maps b–d location is the same as a. The location of the elemental maps k–l is marked in j. The red arrow in a indicates a vacant space in the fracture of pyrite.

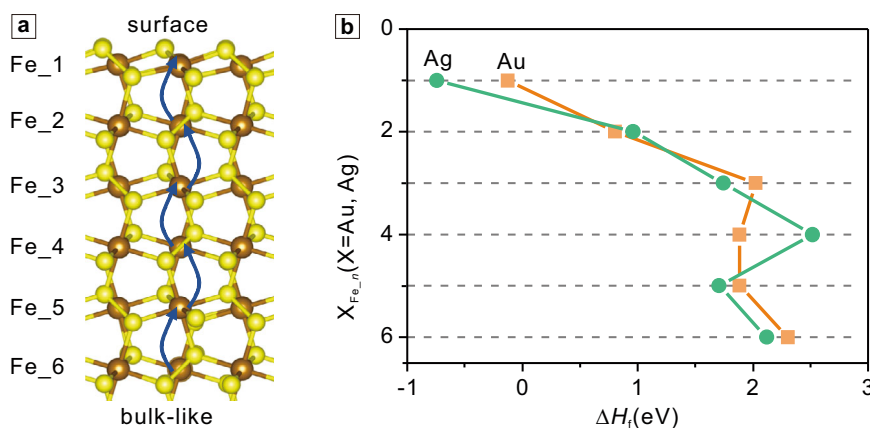


Fig. 3 Thermodynamical properties of gold/silver atoms diffusion from pyrite bulk to the surface. a Schematic of single gold atom substitution on Fe sites in each of the n layers of the pyrite {100} surface. The relative small yellow and large brown spheres denote sulfur and iron atoms, respectively. b Formation enthalpy (ΔH_f) of gold and silver substitution on Fe sites as a function of substitution depth for pyrite {100} surface.

the surface, indicating that the diffusion of bulk lattice-bound Ag/Au atoms to the pyrite surface is thermodynamically favorable.

Discussion

Origin of the nanoparticles. Recent cutting-edge micro- and nano-analytical techniques have evoked a growing recognition of gold^{14–16} and other metallic nanoparticles^{17,18} in pyrite. Two

possible mechanisms may be responsible for forming gold nanoparticles in pyrite¹⁶. One is that the gold nanoparticles were included during pyrite crystallization. The other is that the gold nanoparticles were exsolved after pyrite crystallization and required pre-incorporation of lattice-bound gold ions/atoms in pyrite. In the Dakaitou pyrite, both silver tellurosulfide and gold nanoparticles were observed (Fig. 2e, j–m). Because the partition coefficient of Au(I) between pyrite and the fluid decreases when

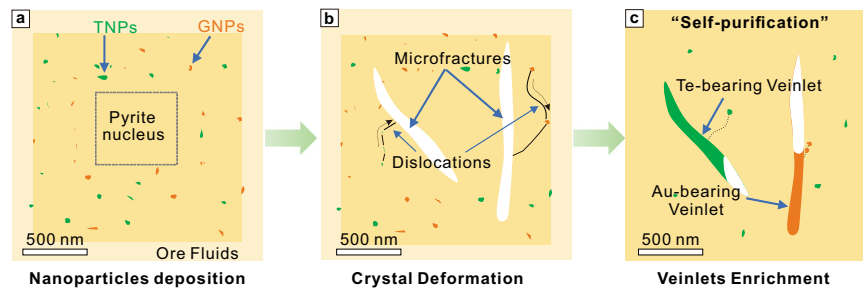


Fig. 4 Illustrations of formation processes of Au-, Ag-, and Te-bearing veinlets in deformed pyrite. **a** Enrichment of gold-bearing nanoparticles (GNPs) and Te-bearing nanoparticles (TNPs); **b** the metamorphism-induced formation of microfractures and dislocations in pyrite; **c** the formation of Au-, Ag-, and Te-bearing veinlets concentrated from the host pyrite through pipe diffusion with dislocations.

temperature increases^{19,20}, gold nanoparticles exsolved from a solid solution at a relatively high temperature is geologically plausible. A previous experimental study demonstrated that gold ions were readily reduced and deposited as nanoparticles at the pyrite–water interface²¹, hence the gold nanoparticles could also be included in pyrite during crystallization (Fig. 4a). Furthermore, the host pyrite may originate from the oriented attachment (OA) of pyrite nanoparticles²² because the host pyrite is composed of nanoparticles (Supplementary Fig. 9a) while it hosts a single crystal structure (Fig. 2f). The gold nanoparticles deposited on the surface of relative large pyrite nanoparticles could thus be fixed at the grain boundaries of pyrite. Taking together, the nanoparticles present in this study most likely were included in pyrite during the crystallization of pyrite via OA.

Formation of veinlets through solid-state elemental migration.

The identical crystallographic orientation of pyrite on both sides of the gold-bearing veinlets in the microfractures (Fig. 2f–g) is evidence of brittle cataclastic deformation^{23,24}. Thus, the fracture-filling gold in orogenic deposits (e.g., the Dakaitou gold deposits shown in Fig. 1) suggests post-ore cataclastic deformation. The widely developed regional fault activities (160 to 110 Ma)²⁵ further suggest that most Jiaodong gold deposits underwent cataclastic deformation during and after gold mineralization at ca. 120 Ma¹². The straight, unreacted pyrite edges exposed to the vacant spaces from sub-micro (red arrow in Fig. 2a) to the nanoscale (Supplementary Fig. 11), and the closed blebs and veinlets suggest that the fractures were not filled with aqueous fluids after its formation. Hence, the interface deposition of gold nanoparticles in the fractures could be excluded. When an aqueous process was absent in the microfractures, the ordered arrangement of the gold nanoparticles at one end of the veinlet (Fig. 2m and Supplementary Movie 3) might record a regional metamorphism-driven migration event along with dislocation as “invisible” gold that can be hosted in dislocations in pyrite²⁶. Thus, the nanoparticles in the host pyrite are the most likely source of veinlets.

The transformation of Au, Ag, and Te in the host pyrite from nanoparticles to veinlets might involve atomic diffusion processes such as pipe diffusion²⁷ or dislocation–impurity pair diffusion^{26,28}. Both crystallization of pyrite via OA and regional metamorphism could produce dislocations for the atomic diffusion of Au, Ag, and Te in the host pyrite (Fig. 4b). The Oswald ripening of gold nanoparticles in pyrite, i.e., the solid-state diffusion of gold, occurs in seconds at temperatures exceeding 370 °C²⁹. Such high diffusivity of gold in pyrite is similar to that of the pipe diffusion of silicon nanoparticles in an aluminum film at 180–480 °C³⁰.

When pipe diffusion is employed, diffusivity (D_p) can be expressed as follows³⁰:

$$D_p = \frac{kT}{2\Omega\gamma S_p} \frac{dV_1}{dt} \left[\frac{1}{r_2} - \frac{1}{r_1} \right]^{-1} \Delta l$$

where Ω is the atomic volume of the diffusion atom, r_i is the radius of precipitate i ($r_1 > r_2$), γ is the surface energy, S_p is the pipe cross-section, dV_1/dt is the volume evolution of precipitate 1, Δl is the distance between precipitates 1 and 2, k is the Boltzmann constant, and T is the temperature. If the diffusion conditions for gold and silver in pyrite were identical, their D_p would be inversely proportional to γ and Ω of gold and silver atoms. Both surface energy (1.50–1.79 J m⁻²) and the van der Waals radii (214 pm) of gold are greater than those of silver (1.12–1.29 J m⁻² and 211 pm)^{31,32}, so the D_p of gold should be smaller than that of silver in pyrite. The calculated ΔH_f of the atomic substitutions of both Au and Ag in different Fe layers (Fig. 3) suggests that the bulk lattice-bound trace elemental atoms have an energetic driving force for diffusion towards the surface, i.e., microfractures in the deformed pyrite (Fig. 4c). Although direct observation of gold atoms leaving gold nanoparticles and diffusing in pyrite is challenging, the thermodynamical properties of gold/silver atoms in pyrite support the spontaneous diffusion of Au/Ag in pyrite from bulk to surface (i.e., fractures) (Fig. 3).

The solid-state transportation of gold from nanoparticles to veinlets present here is different from Ostwald ripening of gold nanoparticles in pyrite^{10,29}, although they can share a solid-state atomic diffusion process. Ostwald ripening describes the process by which gold nanoparticles diffuse from smaller to larger grains in pyrite bulk. However, the solid-state transportation of gold from nanoparticles to veinlets is just an atomic diffusion process from pyrite bulk to surface. It can be defined as a self-purification process³³ because ΔH_f of Au and Ag in pyrite increase with the depth from surface to bulk (Fig. 3). After transportation of Au-Ag and Ag-Te-Fe-S nanoparticles from pyrite bulk to surface (i.e., microfractures), Au can form a melt with Ag and Te (>335 °C)³⁴ in the temperature range of orogenic Au deposits³⁵. The Au-Ag and Ag-Te-Fe-S components then separated when the temperature decreased. This is supported by the curved interface between the two types of veinlets (Fig. 1e).

Another noticeable feature of transforming nanoparticles to veinlets via atomic diffusion is its extremely short timescale³⁰. The theoretical timescale indicates that the atomic diffusion could be very efficient, i.e., it usually completes in a few seconds to minutes³⁰. Note that this only represents the re-enrichment process after forming gold nanoparticles in pyrite. The actual timescale for forming giant gold deposits could be much longer. For example, recent advances in numerical modeling and high-precision dating suggest that hydrothermal pulses likely are short-lived

(<10⁵ years)^{36,37}. We tentatively propose that gold was first deposited during pyrite crystallization as nanoparticles during the magmatic-hydrothermal pulse at a timescale of <10⁵ years, followed by rapid enrichment and upgrading during deformation-induced atomic diffusion. This two-step process could be crucial for forming giant deposits with high grades.

Deformation/thermo-driven self-purification model of concentrating gold nanoparticles to veinlets. We establish a combined deformation/thermo-driven self-purification model of concentrating gold nanoparticles to veinlets in pyrite (Fig. 4). Nanoparticles are initially incorporated into pyrite during crystal growth in ore fluids or exsolution at a relatively high temperature. Subsequent regional metamorphism deforms pyrite, resulting in dislocations and microfractures that provide migration routes and storage spaces. Finally, noble atoms migrate from nanoparticles in bulk pyrite to sub-micro veinlets through atomic diffusion within dislocations, which can be understood as self-purification of pyrite crystals. The formed gold-bearing veinlets can melt with other metals when temperature is appropriate, and then phase separation occurs when temperature decreases. Such a model successfully explains the hyperenrichment of gold from nanoparticles to veinlets and is applicable to any pyrite-containing nanogold when it is deformed by external forces. The model provides insights into understanding the formation of giant gold deposits with high grades. In addition, the rapid solid-state transition may provide an applicable stratagem for gold recovery from refractory ores (e.g., the Carlin-type).

Methods

Electron probe microanalysis. Electron probe microanalysis was performed using a JEOL JXA-8230 Electro-Probe Microanalyzer (EPMA, at Guangzhou Institute of Geochemistry, Chinese Academy of Sciences, GIGCAS) operated at an accelerating voltage of 20 kV and a probe current of 50 nA under a spot size of 1 μm. Peak, upper, and lower background counting times were 20, 10, and 10 s for major elements (Fe and S) and were 40, 20, and 20 for minor elements. Analytical results were reduced using the ZAF (Z, atomic number; A, absorption; F, fluorescence) correction routines. Standard pyrite was used for quantitative calibration of Fe and S, while Ni, Co, Te, Au, Cu, Ag metals, galena (PbS), arsenopyrite (FeAsS), and sphalerite (ZnS) were used for quantitative calibration of minor elements. All standards were from SPI supplies. The pyrite standard was used as a quality monitor standard for the calculation of accuracy and precision of major elements, giving an accuracy of <3%.

SEM-EDS analysis. Backscatter electron images and elemental maps of a polished thin section of the sample were collected using a SEM with a field emission gun (FEG) (JEOL JSM-7001F, at Kyoto University) equipped with EDS (Oxford Instruments, X-Max^N 150 mm²) as well as a desktop SEM (Phenom XL, at electron microscopy center of GIGCAS) equipped with EDS (30 mm²) and operated at 15 kV. The FEG-SEM was operated at 15 kV accelerating voltage and 69 pA emission current with a working distance of ≈10 mm.

Focused ion beam (FIB)-microsampling. A region of interest in a pyrite crystal of the thin section with a box shape (~35 × ~20 × ~35 μm³), was selected by SEM observation and was extracted using FIB microsampling with a Ga⁺ ion source at 30 kV (Thermo Fisher Scientific, Helios NanoLab 3 G CX, and Quanta 200 3DS, at Kyoto University). The sample box was lifted from the thin section and mounted on a W-needle. The mounted sample was analyzed using SR-XCT. After the SR-XCT analysis, the sample was further sliced into thin foils for TEM analyses using the FIB. The sliced thin foils were mounted on TEM grids and thinned to a thickness of ≈100 nm using a Ga⁺ ion source at 30 kV. The surface of the thin foils was cleaned with a Ga⁺ ion source at 2 kV to avoid beam damage and artificial sputtering.

SR-XCT analysis. The SR-XCT imaging experiment was performed at beamline BL47XU of SPring-8, a synchrotron facility in Hyogo, Japan. Three-dimensional successive images were obtained with an X-ray absorption contrast at 7 keV and 900 projections. The voxel size is 60.4 nm, which provides an effective spatial resolution of ~200 nm. The details of this method are reported by Matsumoto et al.³⁸. The stereogram of the SR-XCT data was produced using the tomviz software³⁹.

TEM/STEM-EDS observation and analyses. Thin sections suitable for TEM analyses were extracted from the SR-XCT sample, as mentioned above, by considering the SR-XCT results using FIB microsampling. Both TEM and STEM modes were employed on a Thermo Fisher Scientific FEI Talos F200S TEM (operated at 200 kV) with two windowless EDS detectors (FEI Super-X) at electron microscopy center of GIGCAS. TEM images were captured using a Ceta 16 M camera and analyzed using TEM image analysis (TIA) software (Thermo Fisher Scientific). Nanobeam diffraction patterns were recorded using a 10-μm C2 aperture (which produces a beam size of ~5 nm) under microscope mode in the STEM system. SAED patterns were recorded using a 10 μm selective area aperture (which produces a beam size of ~150 nm) under the microscope mode in the TEM system. The EDS spectra and elemental mappings were recorded using a STEM system. EDS quantifications were performed at a beam current of 1 nA using the Thermo Fisher Scientific TIA software either with or without standards. Standardless quantification was employed for the Ag-Au veinlets. The uncertainties of Ag and Au were <0.2%. Chemically pure Ag₂Te, Ag₂S, and natural pyrite (FeS₂) were employed as standards for the quantification of the Ag-Te-Fe-S veinlets. The uncertainty of Ag, Te, Fe, and S were <0.5%.

μXRD analysis. μXRD patterns of the thin section on a glass slide were recorded in situ using a microbeam diffractometer in reflection mode (Rigaku Dmax Rapid V, Cu Kα, at GIGCAS) operated at 40 kV and 30 mA with a 100-μm collimator for 50 s integration time. The sample stage was rotated with a fixed ω-axis (21°), and φ fluctuated from -30° to 120° (1° per second) to produce the maximum beam footprint of the sample.

DFT calculations. DFT calculations were performed using the Vienna Ab initio Simulation Package⁴⁰ and the projector augmented wave method⁴¹. The PBE + *U* method⁴² (*U* = 1.6 eV) was employed to describe the pyritic surfaces with an energy cutoff of 400 eV for plane wave basis. The feasibility of this method has been confirmed by previous studies on pyritic systems^{21,43,44}. All atoms in the considered pyrite models were fully relaxed until the forces dropped below 0.01 eV/Å. Pyrite {100} surface was selected to simulate fractures because it has the lowest surface energy and thus is the most common cleavage surface during fracturing⁴⁴. The pyrite slabs were modeled using a 2 × 2 supercell with 11 FeS₂ structural layers (88 Fe and 176 S atoms). One Fe atom was substituted by Au or Ag atoms to model the Au/Ag-bearing pyrite. To simulate the Au/Ag atom diffusion near pyrite surfaces, an Fe atom in each considered depth layer was substituted by an Au/Ag atom, similar to the sulfur vacancy diffusion modeling near pyrite surface⁴⁵. The formation enthalpy (Δ*H*_f) of trace elements (i.e., Au and Ag in this study) in various depths of pyrite were calculated using the following equation:

$$\Delta H_f = E_{\text{tpy}} - E_{\text{perf}} - \mu_{\text{Au}} + \mu_{\text{Fe}}$$

where *E*_{tpy} and *E*_{perf} denote the DFT total energies of trace-element substituted pyrite and perfect pyrite, respectively, and *μ*_{Au} and *μ*_{Fe} denote the chemical potentials of Au and Fe atoms in gold and iron metal, respectively.

Data availability

Source data that support the findings of this study are available in figshare with the identifier <https://doi.org/10.6084/m9.figshare.20201063.v146>.

Received: 19 February 2022; Accepted: 15 November 2022;
Published online: 05 December 2022

References

- Phillips, G. N. & Powell, R. Origin of Witwatersrand gold: a metamorphic devolatilisation–hydrothermal replacement model. *Appl. Earth Sci.* **120**, 112–129 (2011).
- Voisey, C. R. et al. Aseismic refinement of orogenic gold systems. *Econ. Geol.* **115**, 33–50 (2020).
- Goldfarb, R., Groves, D. & Gardoll, S. Orogenic gold and geologic time: a global synthesis. *Ore Geol. Rev.* **18**, 1–75 (2001).
- McLeish, D. F., Williams-Jones, A. E., Vasyukova, O. V., Clark, J. R. & Board, W. S. Colloidal transport and flocculation are the cause of the hyperenrichment of gold in nature. *PNAS* **118**, e2100689118 (2021).
- Williams-Jones, A. E., Bowell, R. J. & Migdisov, A. A. Gold in solution. *Elements* **5**, 281–287 (2009).
- Saunders, J. A. Colloidal transport of gold and silica in epithermal precious-metal systems: evidence from the Sleeper deposit. *Nevada. Geol.* **18**, 757–760 (1990).
- Saunders, J. & Burke, M. Formation and aggregation of gold (electrum) nanoparticles in epithermal ores. *Minerals* **7**, 163 (2017).

8. Petrella, L. et al. Colloidal gold transport: a key to high-grade gold mineralization? *Miner. Deposita* **55**, 1247–1254 (2020).
9. Gartman, A. et al. Boiling-induced formation of colloidal gold in black smoker hydrothermal fluids. *Geology* **46**, 39–42 (2018).
10. Hastie, E. C. G., Schindler, M., Kontak, D. J. & Lafrance, B. Transport and coarsening of gold nanoparticles in an orogenic deposit by dissolution–reprecipitation and Ostwald ripening. *Commun. Earth Environ.* **2**, 1–9 (2021).
11. Deng, J. et al. An integrated mineral system model for the gold deposits of the giant Jiaodong province, eastern China. *Earth Sci. Rev.* **208**, 103274 (2020).
12. Qiu, K.-F. et al. Chapter 35: Gold Deposits of the Jiaodong Peninsula, Eastern China. In *Geology of the World's Major Gold Deposits and Provinces*, (eds. Sillitoe, R.H., Goldfarb, R.L., Robert, F. & Simmons, S.F.), pp. 753–774 (Society of Economic Geologists, Littleton, CO, 2020).
13. Zhai, M. et al. Time range of Mesozoic tectonic regime inversion in eastern North China Block. *Sci. China Ser. D Earth Sci.* **47**, 151–159 (2004).
14. Hough, R. M. et al. Naturally occurring gold nanoparticles and nanoplates. *Geol* **36**, 571–574 (2008).
15. Hough, R. M., Noble, R. & Reich, M. Natural gold nanoparticles. *Ore Geol. Rev.* **42**, 55–61 (2011).
16. Palenik, C. S. et al. “Invisible” gold revealed: direct imaging of gold nanoparticles in a Carlin-type deposit. *Am. Mineral.* **89**, 1359–1366 (2004).
17. Ciobanu, C. L. et al. Gold-telluride nanoparticles revealed in arsenic-free pyrite. *Am. Mineral.* **97**, 1515–1518 (2012).
18. Deditius, A. P. et al. Trace metal nanoparticles in pyrite. *Ore Geol. Rev.* **42**, 32–46 (2011).
19. Tauson, V. Gold solubility in the common gold-bearing minerals: experimental evaluation and application to pyrite. *Eur. J. Mineral.* **11**, 937–947 (1999).
20. Pokrovski, G. S. et al. The nature and partitioning of invisible gold in the pyrite-fluid system. *Ore Geol. Rev.* **109**, 545–563 (2019).
21. Xian, H. et al. Crystal habit-directed gold deposition on pyrite: Surface chemical interpretation of the pyrite morphology indicative of gold enrichment. *Geochim. Cosmochim. Acta* **264**, 191–204 (2019).
22. Xian, H. et al. Aggregative growth of quasi-octahedral iron pyrite mesocrystals in a polyol solution through oriented attachment. *CrystEngComm* **18**, 8823–8828 (2016).
23. Barrie, C. D., Pearce, M. A. & Boyle, A. P. Reconstructing the pyrite deformation mechanism map. *Ore Geol. Rev.* **39**, 265–276 (2011).
24. Li, R. et al. The characteristic of microstructural deformation of gold bearing pyrite in Jiaodong: the links between nanoscale gold enrichment and crystal distortion. *Ore Geol. Rev.* **122**, 103495 (2020).
25. Deng, J., Wang, C., Bagas, L., Carranza, E. J. M. & Lu, Y. Cretaceous–Cenozoic tectonic history of the Jiaojia Fault and gold mineralization in the Jiaodong Peninsula, China: constraints from zircon U–Pb, illite K–Ar, and apatite fission track thermochronometry. *Miner. Deposita* **50**, 987–1006 (2015).
26. Fougereuse, D. et al. A new kind of invisible gold in pyrite hosted in deformation-related dislocations. *Geology* **49**, 1225–1229 (2021).
27. Piazzolo, S. et al. Deformation-induced trace element redistribution in zircon revealed using atom probe tomography. *Nat. Commun.* **7**, 10490 (2016).
28. Dubosq, R., Rogowitz, A., Schweinar, K., Gault, B. & Schneider, D. A. A 2D and 3D nanostructural study of naturally deformed pyrite: assessing the links between trace element mobility and defect structures. *Contrib. Mineral. Petrol.* **174**, 1–16 (2019).
29. Reich, M. et al. Thermal behavior of metal nanoparticles in geologic materials. *Geol* **34**, 1033–1036 (2006).
30. Legros, M., Dehm, G., Arzt, E. & Balk, T. J. Observation of giant diffusivity along dislocation cores. *Science* **319**, 1646–1649 (2008).
31. Skriver, H.L. & Rosengard, N.M. Surface energy and work function of elemental metals. *Phys. Rev. B: Condens. Matter* **46**, 7157–7168 (1992).
32. Hu, S.-Z., Zhou, Z.-H. & Robertson, B. E. Consistent approaches to van der Waals radii for the metallic elements. *Z. Kristallogr. Krist.* **224**, 375–383 (2009).
33. Dalpian, G. M. & Chelikowsky, J. R. Self-purification in semiconductor nanocrystals. *Phys. Rev. Lett.* **96**, 226802 (2006).
34. Cabri, L. J. Phase relations in the Au–Ag–Te systems and their mineralogical significance. *Econ. Geol.* **60**, 1569–1606 (1965).
35. Tomkins, A. G., Pattison, D. R. M. & Zaleski, E. The Hemlo gold deposit, Ontario: an example of melting and mobilization of a precious metal-sulfosalt assemblage during amphibolite facies metamorphism and deformation. *Econ. Geol.* **99**, 1063–1084 (2004).
36. Weis, P., Driesner, T. & Heinrich, C. A. Porphyry-copper ore shells form at stable pressure-temperature fronts within dynamic fluid plumes. *Science* **338**, 1613–1616 (2012).
37. Li, Y., Li, X.-H., Selby, D. & Li, J.-W. Pulsed magmatic fluid release for the formation of porphyry deposits: Tracing fluid evolution in absolute time from the Tibetan Qulong Cu–Mo deposit. *Geology* **46**, 7–10 (2018).
38. Matsumoto, M. et al. Discovery of fossil asteroidal ice in primitive meteorite Acfer 094. *Sci. Adv.* **5**, eaax5078 (2019).
39. Hanwell, M. D. et al. Tomviz: open source platform connecting image processing pipelines to GPU accelerated 3D visualization. *Microsc. Microanal.* **25**, 408–409 (2019).
40. Kresse, G. & Furthmüller, J. Efficiency of ab-initio total energy calculations for metals and semiconductors using a plane-wave basis set. *Comput. Mater. Sci.* **6**, 15–50 (1996).
41. Kresse, G. & Joubert, D. From ultrasoft pseudopotentials to the projector augmented-wave method. *Phys. Rev. B* **59**, 1758–1775 (1999).
42. Dudarev, S. L., Botton, G. A., Savrasov, S. Y., Humphreys, C. J. & Sutton, A. P. Electron-energy-loss spectra and the structural stability of nickel oxide: an LSDA+U study. *Phys. Rev. B* **57**, 1505–1509 (1998).
43. Xian, H. et al. The mechanism of defect induced hydroxylation on pyrite surfaces and implications for hydroxyl radical generation in prebiotic chemistry. *Geochim. Cosmochim. Acta* **244**, 163–172 (2019).
44. Xian, H. et al. Environmental-sulfur-controlled surface properties of pyrite: a first principles PBE + U study. *Phys. Chem. Min.* **48**, 20 (2021).
45. Zhang, Y. N., Law, M. & Wu, R. Q. Atomistic modeling of sulfur vacancy diffusion near iron pyrite surfaces. *J. Phys. Chem. C* **119**, 24859–24864 (2015).
46. Xian, H. Raw data for “Hyperenrichment of gold in pyrite induced by solid-state transportation”. <https://doi.org/10.6084/m9.figshare.20201063.v1> (2022).

Acknowledgements

We thank Dr. Evan Hastie and two anonymous reviewers for their constructive comments and suggestions on the manuscript. This study was financially supported by the National Key R & D Program of China (2018YFA0702600), National Natural Science Foundation of China (42130801, 42072087), Guangdong Basic and Applied Basic Research Foundation (2022B1515020007 & 2019A1515011303), Youth Innovation Promotion Association CAS (2021353), and Tuguangchi Award for Excellent Young Scholar GIGCAS. This is contribution No. IS-3267 from GIGCAS.

Author contributions

Conceptualization: H.X., H.H., and J.Z. SEM, TEM, and FIB works: H.X., Y.Y., J.X., A.Ts., M.Y., S.E., and A.M. SR-XCT works: A.Ts., M.Y., and S.E. μ XRD works: H.X. & J.X. EPMA works: H.X. & K.Q. DFT calculations: H.X. & R.Z. Data Analysis: H.X., H.H., J.Z., W.T., Y.L., and A.Ts. Writing—original draft: H.X. & H.H. Writing—review & editing: all authors.

Competing interests

The authors declare no competing interests.

Additional information

Supplementary information The online version contains supplementary material available at <https://doi.org/10.1038/s43247-022-00628-x>.

Correspondence and requests for materials should be addressed to Hongping He.

Peer review information *Communications Earth & Environment* thanks Evan Hastie and the other, anonymous, reviewer(s) for their contribution to the peer review of this work. Primary Handling Editor: Joe Aslin. Peer reviewer reports are available.

Reprints and permission information is available at <http://www.nature.com/reprints>

Publisher's note Springer Nature remains neutral with regard to jurisdictional claims in published maps and institutional affiliations.



Open Access This article is licensed under a Creative Commons Attribution 4.0 International License, which permits use, sharing, adaptation, distribution and reproduction in any medium or format, as long as you give appropriate credit to the original author(s) and the source, provide a link to the Creative Commons license, and indicate if changes were made. The images or other third party material in this article are included in the article's Creative Commons license, unless indicated otherwise in a credit line to the material. If material is not included in the article's Creative Commons license and your intended use is not permitted by statutory regulation or exceeds the permitted use, you will need to obtain permission directly from the copyright holder. To view a copy of this license, visit <http://creativecommons.org/licenses/by/4.0/>.

© The Author(s) 2022